TIME-DOMAIN ACOUSTIC FULL-WAVEFORM INVERSION BASED ON DUAL-SENSOR SEISMIC ACQUISITION SYSTEM

YU ZHONG[1] and YANGTING LIU [2,3]

[1] *School of Geophysics and Information Technology, China University of Geosciences, Beijing 100083, P.R. China. zhongyu26happy@163.com*
[2] *First institute of Oceanography, Ministry of Natural Resources, Qingdao 266061, P.R. China. yangting.lau@gmail.com*
[3] *Qingdao National Laboratory for Marine Science and Technology, Qingdao 266061, P.R. China.*

(Received April 25, 2018; revised version accepted January 20, 2019)

ABSTRACT

Zhong, Y. and Liu, Y.T., 2019. Time-domain acoustic full-waveform inversion based on dual-sensor seismic acquisition system. *Journal of Seismic Exploration*, 28: 103-120.

In many previous studies, attentions were paid to using dual-sensor seismic acquisition system for suppressing ghost waves, extending seismic bandwidth and improving resolution of migration, while few attentions were paid to full-waveform inversion (FWI) based on dual-sensor's seismic data. In this paper, we propose an acoustic FWI method based on dual-sensor acquisition system. We first review conventional acoustic FWI and compare it with our new dual-sensor acoustic FWI. Then we give the boundary condition for our dual-sensor acoustic FWI. Secondly, we derive new gradient equations with the spatial derivative of particle velocities replaced by the time derivative of pressure. Further, time-domain multi-scale strategy is conducted to reduce the nonlinearity of acoustic FWI. At last, the synthetic examples of modified Marmousi model are presented to demonstrate the efficiency and advantages of our dual-sensor acoustic FWI over conventional acoustic FWI. It can be found that, compared with conventional acoustic FWI, dual-sensor acoustic FWI almost does not cause extra computation and memory costs but can improve the accuracy of acoustic FWI.

KEY WORDS: dual-sensor seismic acquisition system, dual-sensor FWI, boundary conditions.

0963-0651/19/$5.00

INTRODUCTION

Full waveform inversion (FWI) is a method in retrieving high-resolution subsurface parameters from seismic data and has been extensively developed by many researchers (Lailly, 1983; Tarantola, 1984, 1986; Mora, 1987; Sirgue and Pratt, 2004; Sears et al., 2008; Virieux and Operto, 2009). Although acoustic FWI and elastic FWI are both widely adopted to reconstruct the subsurface compressional velocity, elastic FWI seems more suitable than acoustic FWI since elastic FWI can reconstruct additional shear wave velocity model. The shear wave velocity model is important for reservoir characterization, quantitative imaging (Brossier et al., 2009a,b) and interpretation of the dynamics of the reflection data (Plessix and Cao, 2011). However, the compressional velocity models from elastic FWI are often worse than that from acoustic FWI because of that the trade-off effects of shear velocity models; the interference of different kinds of wave modes also contribute to degraded inverted compressional velocity models of elastic FWI (Tarantola, 1986; Virieux and Operto, 2009). In addition, it is expensive to get multi-component elastic seismic data for elastic FWI. Thus, it is more difficult to obtain high resolution compressional velocity models by elastic FWI when compared with acoustic FWI.

Suitable gradient equations are important for giving right decrease direction of the objective function, proper evaluation of the step length and termination criteria in gradient-based optimization methods (Baumsteinet et al., 2009). Tarantola (1986) first derived elastic parameters' gradients based on second-order displacement equations. Crase et al. (1990) proposed a more robust objective function, and they used first-order velocity-stress equations to calculate the forward wave-field and derived corresponding adjoint equations. But they still used the gradients equations of Tarantola (1986) to update the parameters. Shipp et al. (2002) inverted compressional velocities using large angle reflection data of ocean. They also used first-order velocity-stress equations to calculate the forward wave-field and replaced the displacement' spatial derivative of velocity by pressure to improve the computational efficiency of FWI. Liu et al. (2006) deduced the adjoint equations and the gradient equations by Lagrange multiplier method. Zhou et al. (2008) and Wang et al. (2012) used adjoint state method to derivate adjoint equations and new gradient equations which are suitable for the first-order velocity-stress elastic wave equations.

The two-way acoustic wave equation for FWI is a second-order spatial partial differential equation. Theoretically, it needs two spatial boundary conditions to solve two-way wave equation in the depth domain (Sandberg and Beylkin, 2009). But conventional seismic acquisition system only received the wave-field at one given depth. Therefore, it is an underdetermined problem to solve two-way acoustic wave equation using the spatial boundary condition provided by current seismic acquisition system. Based on this problem, some previous studies (Vasconcelos, 2013; Ravasi et al., 2015a,b; You et al., 2016) proposed dual-sensor seismic acquisition system to record seismic data and then completely solved the full wave equation in depth domain based on two layers' data. They got

high-resolution and true-amplitude depth migration profiles. In fact, marine towed-streamers acquisition system similar to the dual-sensor seismic acquisition, firstly proposed by Sonneland et al. (1986), was used earlier for suppressing weather noise and separating up-going and down-going wave-field. However, it was difficult to hold two streamers at the same vertical plane limited by the techniques at that time. With the development of marine seismic acquisition techniques, it is not a difficult problem now. In previous research, the marine towed-streamers acquisition system was used for suppressing ghost waves, extending seismic bandwidth (Hill et al., 2006; Özdemir et al., 2008), and improving resolution of migration (Moldoveanu et al., 2007; Bunting et al., 2011). You et al. (2017) implemented RTM based on dual-sensor seismic acquisition system and got a higher resolution result than conventional RTM. The main reason is that the backward wave-field in the time domain can be more accurately extrapolated when suitable spatial boundary conditions and initial conditions are provided by dual-sensor seismic acquisition system. However, few of them paid attentions to the FWI based on the dual-sensor seismic acquisition system.

Therefore, this study conducts acoustic FWI with suitable spatial boundary conditions and initial conditions, which are provided by dual-sensor seismic acquisition system. We can reconstruct more accurate and stable parameters based on the data from dual-sensor seismic acquisition system than that based on single sensor's record. Inversion tests using the synthetic data of a modified Marmousi model are implemented to prove the feasibility and correctness of our algorithm. The structure of this paper is as follows: Firstly, we begin with a brief introduction to our dual-sensor FWI and propose different boundary condition. Secondly, we deduce new gradients of model parameters and introduce time domain multi-scale strategy. Then we combine these strategies and implement our dual-sensor FWI, using the synthetic data of a modified Marmousi model, which demonstrates our dual-sensor FWI is effective. Finally, we give some conclusions.

THEORY

Time-domain Dual-Sensor FWI

The 2D acoustic velocity-stress equations in Cartesian coordinate system are expressed as (Virieux, 1984) with the initial and boundary conditions:

$$\begin{cases} \dfrac{\partial V_x}{\partial t} = \dfrac{1}{\rho}\dfrac{\partial P}{\partial x}. \\ \dfrac{\partial V_z}{\partial t} = \dfrac{1}{\rho}\dfrac{\partial P}{\partial z}. \\ \dfrac{\partial P}{\partial t} = \kappa\left(\dfrac{\partial V_x}{\partial x} + \dfrac{\partial V_z}{\partial z}\right) + f. \\ V_x(x,z,t<0) = 0, V_z(x,z,t<0) = 0, P(x,z,t<0) = 0, f = \varphi(t)\delta(x - x_s, z - z_s). \end{cases} \tag{1}$$

where V_x is the horizontal particle velocity, V_z is the vertical particle velocity, P is the pressure, f is the source item, $\varphi(t)$ is the source function, (x_s, z_s) are coordinates of the source, ρ is the density, and κ is the bulk modulus ($\kappa = \rho V_P^2$, V_P is the compressional velocity), respectively.

In our acoustic FWI, the objective function is set as L_2 objective function:

$$E = \frac{1}{2}\left\| P(m)^{cal} - P^{obs} \right\|_2^2 , \tag{2}$$

where $P^{cal}(m)$ is calculated pressure data with model m, and P^{obs} is the observed pressure data, respectively.

According to the adjoint state method (Liu and Tromp, 2006; Wang et al., 2012), the following adjoint state wave eqs. (3) corresponding to acoustic first-order velocity-stress eqs. (1) can be derived (Appendix) as:

$$\begin{cases} \rho \dfrac{\partial u_x}{\partial t} = \kappa \dfrac{\partial p}{\partial x}. \\ \rho \dfrac{\partial u_z}{\partial t} = \kappa \dfrac{\partial p}{\partial z}. \\ \dfrac{\partial p}{\partial t} = (\dfrac{\partial u_x}{\partial x} + \dfrac{\partial u_z}{\partial z}). \end{cases} \tag{3}$$

With the marine dual-sensor seismic acquisition system, shown in Fig. 1, where two streamers at different depths ($z1$ and $z2$) below the sea surface are towed behind a survey vessel, the final and boundary conditions can be written as:

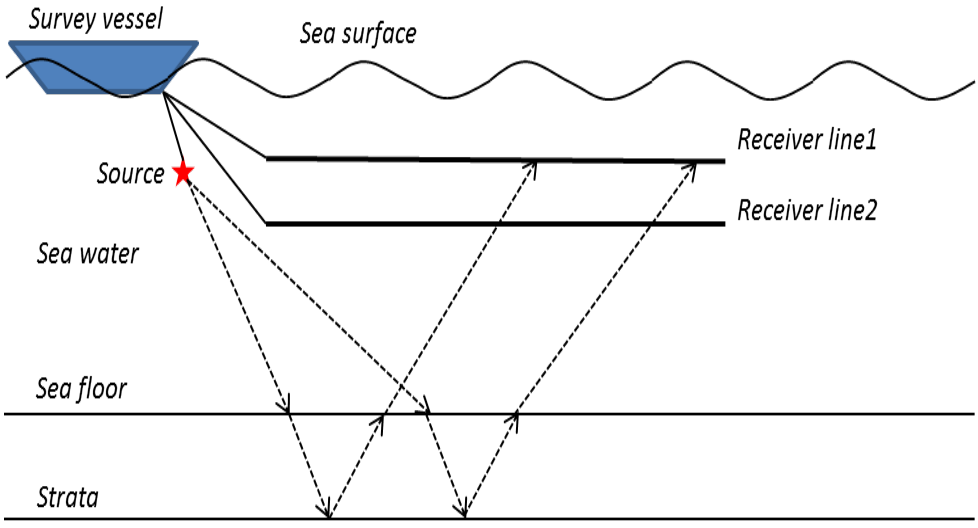

Fig. 1. Marine dual-sensor seismic acquisition system.

$$\begin{cases} p(x,z1,t) = P^{cal}(x,z1,t) - P^{obs}(x,z1,t). \\ p(x,z2,t) = P^{cal}(x,z2,t) - P^{obs}(x,z2,t). \\ u_x(x,z,t>T) = 0. \\ u_z(x,z,t>T) = 0. \\ p(x,z,t>T) = 0. \end{cases} \tag{4}$$

where u_x is the adjoint horizontal particle velocity, u_z is the vertical particle velocity, p is the adjoint pressure, $P^{cal}(x,z1,t) - P^{obs}(x,z1,t)$, $P^{cal}(x,z2,t) - P^{obs}(x,z2,t)$ are the residuals of the pressure between the calculated data and observed data at two different depths, and T is the maximum of recording time, respectively.

In conventional acoustic FWI, it is usually assumed the final condition and boundary condition as:

$$\begin{cases} p(x,z1,t) = P^{cal}(x,z1,t) - P^{obs}(x,z1,t). \\ u_x(x,z,t>T) = 0. \\ u_z(x,z,t>T) = 0. \\ p(x,z,t>T) = 0. \end{cases} \tag{5}$$

The residual of pressure record from single sensor acts as virtual sources to back propagate upward and downward from the boundary points from maximum time to minimum time, disregarding the direction from which it arrived, thus creating some artificial adjoint state wave-field by conventional conditions eqs. (5). Although the absorbing boundary can be used to attenuate the upward wave-field, the downward wave-field is mirrored back-propagated downward instead of upward. This mirrored back-propagated downward will creating some strong artificial noncausal adjoint state wave-field. Thus, the adjoint state wave-field is inaccurate under the conventional conditions eqs. (5). Instead the boundary conditions eqs. (4) can stack and reduce the energy of artificial noncausal adjoint state wave-field. Therefore we use final and boundary conditions eqs. (4) to improve the accuracy of adjoint state wave-field.

The detailed steps to calculate the gradients of parameters of our time domain dual-sensor FWI are as follows: Firstly, numerically solve eqs. (1) with the initial conditions from minimum time to maximum time to obtain the forward source wave-field and store the wave-field at the boundary region. Secondly, back propagate the residuals record by solving eqs. (3) with the final and boundary conditions equations to get the adjoint state wave-field and reconstruct the source wave-field by boundary reconstruct method from maximum time to minimum time. With two order of time, high order of space staggered grid finite difference to solve eqs. (1) and eqs. (3), followed by the perfectly matched layer to eliminate the boundary reflection,

thirdly, we cross-correlate the adjoint state wave-field and the source wave-field to calculate the gradients of density and bulk modulus using following equations (see the Appendix):

$$\begin{cases} \dfrac{\partial E}{\partial \rho} = -\sum\limits_{is=1}^{ns} \int_0^T (u_x \dfrac{\partial V_x}{\partial t} + u_z \dfrac{\partial V_z}{\partial t}) dt. \\ \dfrac{\partial E}{\partial \kappa} = \sum\limits_{is=1}^{ns} \int_0^T p(\dfrac{\partial V_x}{\partial x} + \dfrac{\partial V_z}{\partial z}) dt. \end{cases} \tag{6}$$

Since the following equation:

$$\frac{\partial P}{\partial t} = \rho V_P^2 (\frac{\partial V_x}{\partial x} + \frac{\partial V_z}{\partial z}) \quad . \tag{7}$$

We can further derive the new gradient equations as

$$\begin{cases} \dfrac{\partial E}{\partial \rho} = -\sum\limits_{is=1}^{ns} \int_0^T (u_x \dfrac{\partial V_x}{\partial t} + u_z \dfrac{\partial V_z}{\partial t}) dt. \\ \dfrac{\partial E}{\partial \kappa} = \sum\limits_{is=1}^{ns} \int_0^T (p \dfrac{\partial P}{\partial t}) / \kappa) dt. \end{cases} \tag{8}$$

The new gradients eqs. (8) use time derivative of pressure to replace the spatial derivative of particle velocity. And the new gradient eqs. (8) can reduce the calculation time and improve the accuracy of gradients compared with the old gradient eqs. (6). Shipp et al. (2002) applied a similar method, in which the displacement' spatial derivative was replaced by pressure, to improve the computational efficiency of FWI.

To decrease the nonlinearity of FWI, multi-scale strategies are usually implemented in time domain (Bunks et al., 1995; Boonyasiriwat et al., 2009), frequency domain (Pratt et al., 1998; Brossier et al., 2009), or hybrid domain (Sirgue et al., 2008). Here, we use Wiener filter instead of low-pass filter to improve the accuracy of time domain multi-scale strategy (Boonyasiriwat et al., 2009), which can be computed by

$$F_{Wiener}(\omega) = \frac{W^*_{origional}(\omega) W_{Target}(\omega)}{\left| W_{original}(\omega) \right|^2 + \varepsilon^2} \quad , \tag{9}$$

where $F_{Wiener}(\omega)$ is the Wiener filter, $W_{original}$ is the original wavelet, W_{target} is the low-frequency target wavelet, ω is the angular frequency, ε is a small parameter that prevents numerical overflow, and * denotes the complex conjugate.

According to the chain rule for compound function's derivation and the velocity and density relationships with bulk modulus

$$V_p = \sqrt{\frac{\kappa}{\rho}}, \kappa = \rho V_p^{\ 2} \quad . \tag{10}$$

We can present the gradient equations for compressional velocity and density as

$$\begin{cases} \dfrac{\partial E}{\partial V_p} = \dfrac{\partial E}{\partial \kappa}\dfrac{\partial \kappa}{\partial V_p} + \dfrac{\partial E}{\partial \rho}\dfrac{\partial \rho}{\partial V_p} = 2\rho V_p \dfrac{\partial E}{\partial \kappa}. \\ \dfrac{\partial E}{\partial \rho} = \dfrac{\partial E}{\partial \rho} + \dfrac{\partial E}{\partial \kappa}\dfrac{\partial \kappa}{\partial \rho} = \dfrac{\partial E}{\partial \rho} + V_p^{\ 2}\dfrac{\partial E}{\partial \kappa}. \end{cases} \tag{11}$$

And then the gradient-based methods can be applied to update the model parameters through iterations with the form

$$m^{k+1} = m^k + \alpha^k d^k \quad , \tag{12}$$

where m^k and m^{k+1} are the model parameter vectors at current and next iteration, respectively; α^k is current update step length, which can be computed using line search algorithm (Nocedal and Wright, 2006); d^k is the current update direction of model parameter vectors.

INVERSION EXAMPLES

In this section, one synthetic example is used to certify the effectiveness and advantages of our dual-sensor FWI method over conventional acoustic FWI. For simplicity, the free surface effects (multiple, conversion, and surface waves) are not considered, and the source wavelet is known in our examples.

We resample and downsize the Marmousi model to reduce the computational cost. And the true compressional velocity model and density model are shown in Figs. 2(a) and 2(c). The density model is 0.8 times of the compressional velocity model. The model dimension is 5390 m ×1290 m with grid steps of 10 m×10 m. There are 34 shots located at a depth 20 m with the space interval of 160 m. And 540 receivers are put at the depth z = 20 m and z = 30 m with the space interval of 10 m to record the wave-field of pressure, respectively. In the modeling and FWI, the Ricker wavelet, with a domain frequency of 20 Hz, is used as the source. The sampling interval is 0.001 s, and the length of record time is 2.5 s. The initial compressional velocities and densities, as shown in Figs. 2(b) and 2(d), are yielded by a smooth operator (the size of 500 m × 500 m) of the true models. In this

example, time-domain multi-scale FWI is used to avoid local minimum, and the inversion is divided into four stages with the frequency bands 0–5, 0–10, 0–15 and 0–20 Hz. The conjugate gradient is used to update the model.

To evaluate the quality of the FWI, we estimate the relative errors between the inverted models and the true ones by

$$error_{model} = \sqrt{\frac{1}{nx * nz}\left\| \frac{m_{inverted} - m_{true}}{m_{true}} \right\|_2^2}, \tag{14}$$

where m_{true} and $m_{inverted}$ are the true and inverted parameter, respectively, with the dimension of $nx * nz$. If the value of $error_{model}$ is smaller, the inversion accuracy is higher.

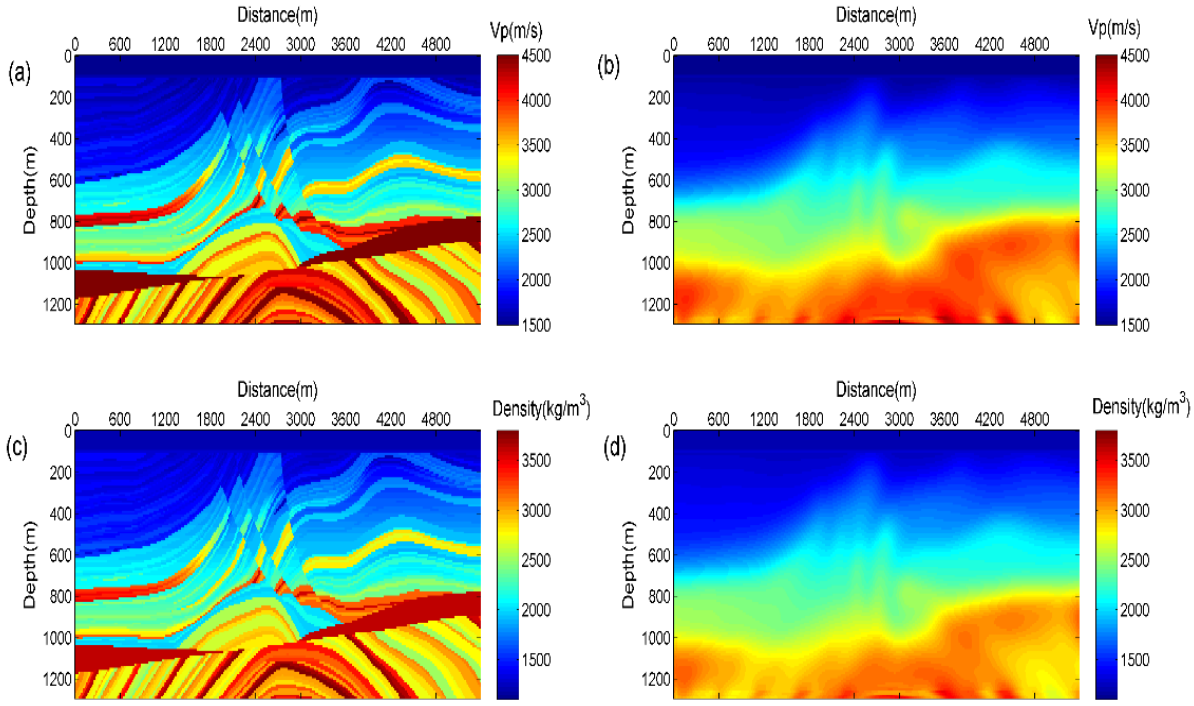

Fig. 2. A modified Marmousi2 model: (a) The true compressional velocity model, (b) the initial compressional velocity model, (c) the true density model, and (d) the initial density model.

Inversion with different gradient equations based on the data provided by dual-sensor

In order to test the accuracy and efficiency of the FWI by the different gradient equations, we first use the old gradient eqs. (6) and new gradient eqs. (8) to invert compressional velocity and density simultaneously, respectively. The pressure seismic data at two different depths, provided by dual-sensor seismic acquisition system, is used. All the other conditions are the same during the inversion except the gradient equations.

Fig. 3 displays the inverted velocity models and density models by different gradient equations. From Figs 3(a) - 3(d), it can be seen that both of the reconstructed compressional velocities and densities by different gradient equations are in good accordance with each other not only in structure but also in model values. While the inverted results of the FWI by new gradient eqs. (8) have slightly better resolution than the results of the FWI by old gradient eqs. (6) especially in some areas (for example in the black ellipse) from Figs 3(a) - 3(d).

It indicates that the reconstructed compressional velocity and density by new gradient equations (8) are slightly accurate than that by the old gradient equations (6). In addition, the acoustic FWI by new gradient equations (8) cost less time compared with that by old gradient equations (6) under the same calculation condition. So we implement acoustic FWI by new gradient equations in the following part.

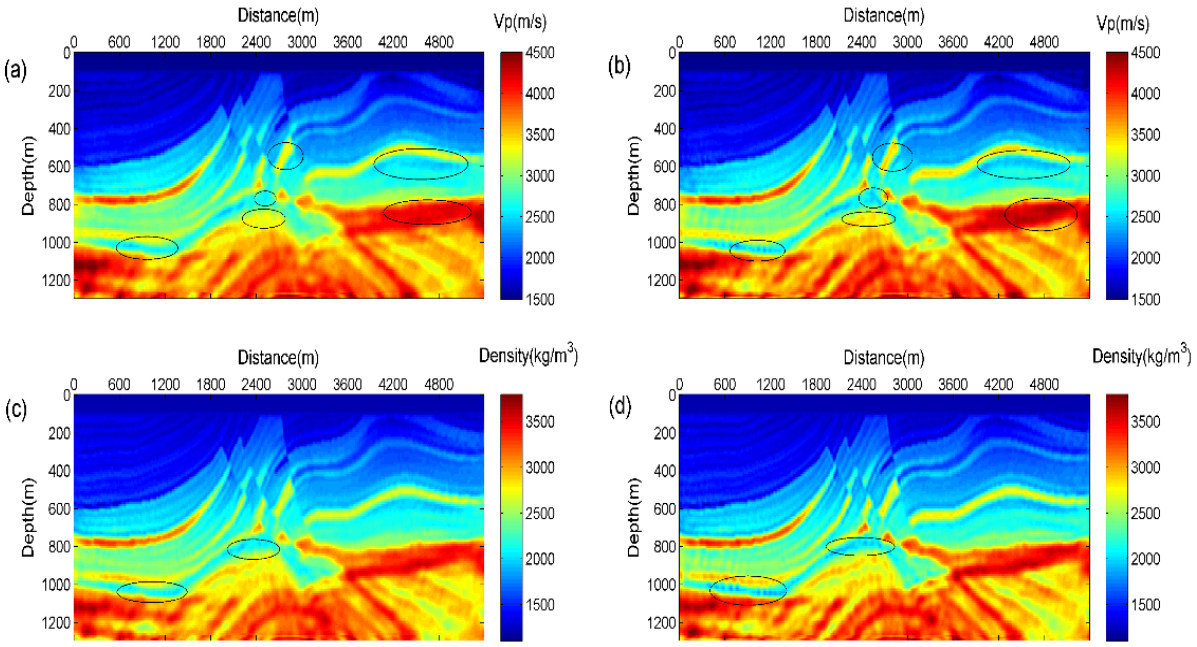

Fig. 3. Inverted models based on different gradient equations by dual-sensor: (a) the inverted compressional velocity model by old gradient equation, (b) the inverted compressional velocity model by new gradient equation, (c) the inverted density model by old gradient equation, and (d) the inverted density model by new gradient equation.

Inversions based on data at different depth provided by single sensor

To test the effectiveness and advantage of our new dual-sensor FWI over conventional acoustic FWI, we then use the pressure seismic data at different depths provided by single sensor to invert the models. And the new gradient equations are used to invert compressional velocity and density simultaneously.

The inversion results are displayed in Fig. 4, where Figs. 4(a) and 4(b) show the inverted compressional velocities, and Figs. 4(c) and 4(d) display

the inverted densities. Comparisons of the Figs. 4(a) and 4(b) with Fig. 3(b) indicate that the reconstructed compressional velocities by single sensor's record at different depths are worse than that by dual-sensor's record. There are some artificial results especially in the black ellipse area in Figs. 4(a) and 4(b). The reconstructed densities by single sensor are in good accordance with that by dual-sensor not only in structure but also in model values from Figs. 4(c), 4(d) and 3(d).

And the normalized gradients of the parameters at the first iteration, with the 20 Hz dominant frequency wavelet, are shown in Fig. 5, where Figs. 5(a), 5(c) and 5(e) show the gradient models of compressional velocity, and Figs. 5(b), 5(d) and 5(f) display the gradient models of density. From the Fig. 5, it can be seen that the gradient model of compressional velocity based on the dual-sensor have higher resolution when compared with that based on the singer sensor especially in the black ellipse area in Figs. 5(a), 5(c) and 5(e). The gradient model density by single sensor is in good accordance with that by dual-single from Figs. 5(b), 5(d) and 5(f).

More inversion details can be seen from Fig. 6 that illustrates the inverted results at the distance of 2.59 km, 3.15 km and 4.5 km. In Fig. 6 the inverted results based on the data provided by the first layer's singer sensor are denoted by "Scheme 1", the inverted results based on the data provided by the second layer's singer sensor are denoted by "Scheme 2", and inverted results based on the data provided by the dual-sensor are denoted by "Scheme 3".

It is easy to observe that inverted results based on the data provided by the dual-sensor are closer to the true models than that based on the data provided by the singer sensor. Also as shown in Table 1, the relative errors based on first layer's single sensor's record, second layer's single sensor's record and dual-sensor's record for compressional velocities are 0.0682 and 0.0687, and 0.0610, respectively; And the relative errors for densities are 0.0644 and 0.0647, and 0.0632, respectively. It's clear that the accuracy of our dual-sensor FWI is higher than that of conventional acoustic FWI. In addition, there is almost no increase in computation and memory costs of our dual-sensor FWI when compared with conventional acoustic FWI because the number of the wave-field variables does not change.

Table 1. Inverted errors based on the data provided by the single and dual sensor.

Parameter	Inverted error for first layer's single sensor	Inverted error for second layer's single sensor	Inverted error for dual sensor
V_p	0.0682	0.0687	0.0610
ρ	0.0644	0.0647	0.0632

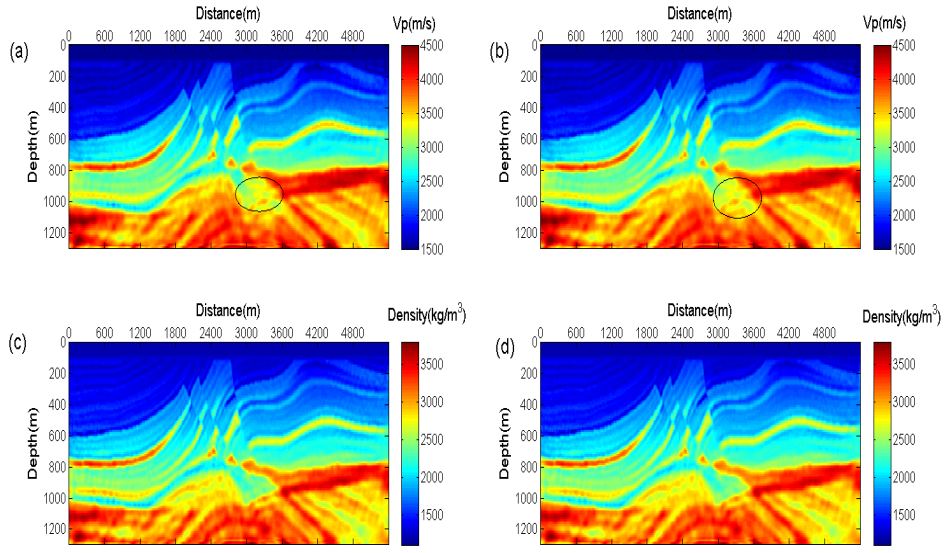

Fig. 4. Inverted models using new gradient equations based on the data provided by the single sensor: (a) the inverted compressional velocity based on the data provided by first layer's singer sensor, (b) the inverted compressional velocity based on the data provided by second layer's single sensor, (c) the inverted density based on the data provided by first layer's singer sensor, and (d) the inverted density based on the data provided by second layer's single sensor.

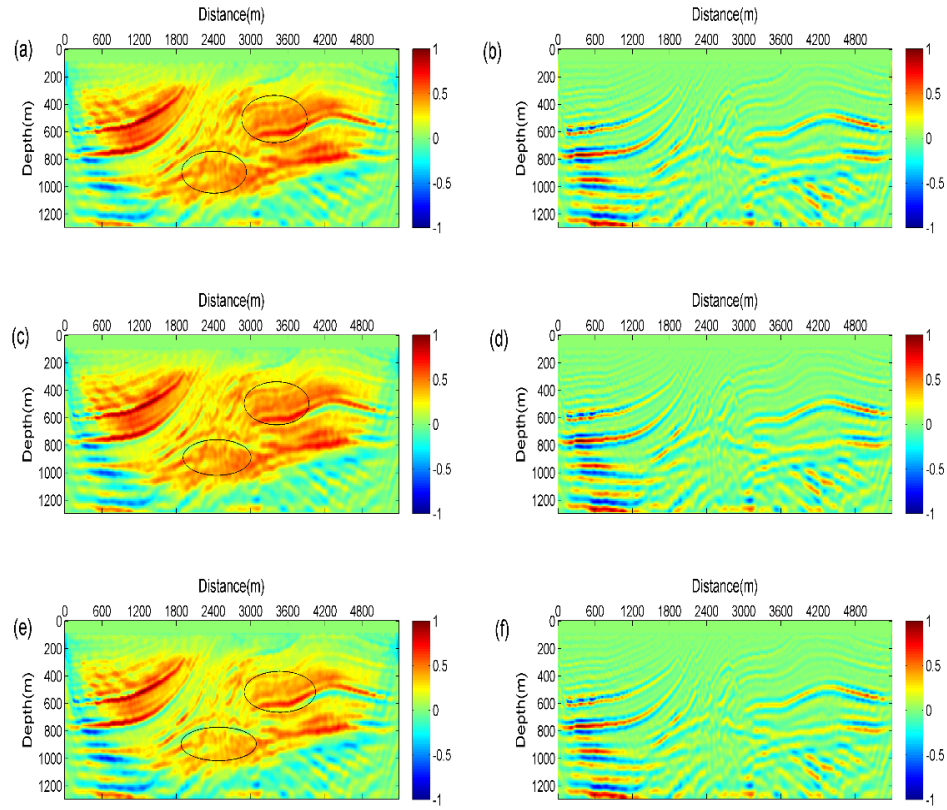

Fig. 5. The normalized gradient models of compressional velocity and density at the first iteration: (a) the gradient of compressional velocity based on the data provided by first layer's singer sensor, (b) the gradient of density based on the data provided by first layer's singer sensor, (c) the gradient of compressional velocity based on the data provided by second layer's single sensor, (d) the gradient of density based on the data provided by second layer's single sensor, (e) the gradient of compressional velocity based on the data provided by dual-sensor seismic acquisition system, and (f) the density gradient based on the data provided by dual-sensor seismic acquisition system.

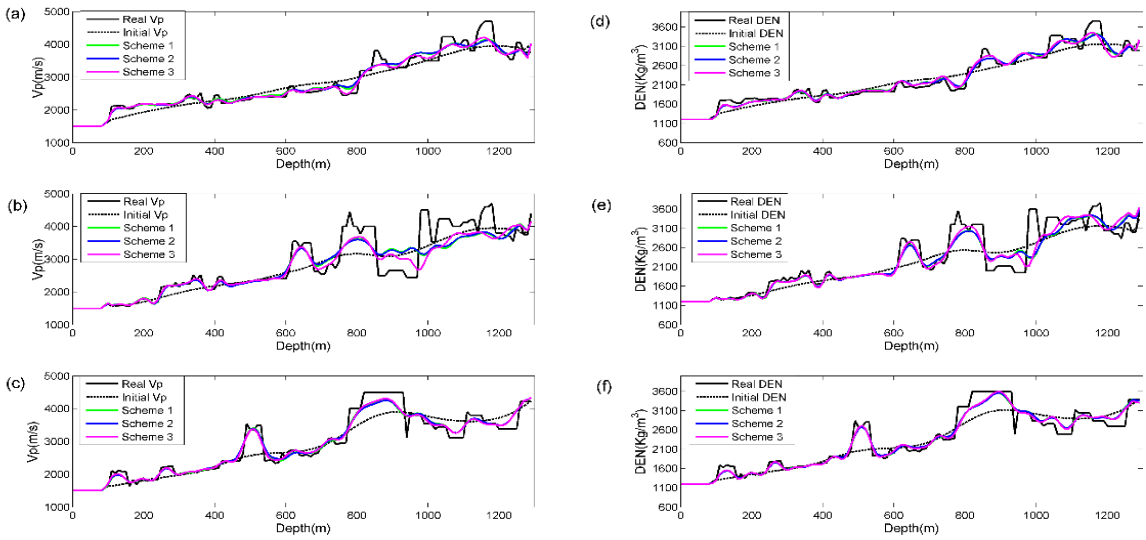

Fig. 6. Inverted results based on the data provided by the single and dual sensor. Panels (a-c) show the inverted compressional velocity at the distance of 2.59 km, 3.15 km and 4.5 km, respectively. Panels (d-f) show the inverted density at the distance of 2.59 km, 3.15 km and 4.5 km, respectively.

CONCLUSION

In this paper, we have introduced the time-domain dual-sensor acoustic FWI and proposed some inversion strategies. The main idea is based on dual-sensor data from the marine dual-sensor seismic acquisition system. The adjoint state wave-field based on the boundary conditions provided by marine dual-sensor seismic acquisition system is more accurate than that based on the boundary conditions provided by conventional single sensor seismic acquisition system. Thus, dual-sensor acoustic FWI can estimate more accurate parameter models than conventional acoustic FWI. The test of a modified Marmousi model reveal that there are some advantages of dual-sensor acoustic FWI over conventional acoustic FWI. Our dual-sensor acoustic FWI is, therefore, promising to make use of dual-sensor's seismic data.

ACKNOWLEDGEMENT

This study was funded by National Natural Science Foundation of China (Grant No. 41804131), Basic Scientific Fund for National Public Research Institutes of China (Grant No. 2018Q02), Shandong Provincial Natural Science Foundation, China (Grant No. ZR2018QD003), and Qingdao National Laboratory for Marine Science and Technology (Grant No. QNLM201710). Thanks should also be given the anonymous reviewer and Dr. Fengxia Gao for their English writing suggestions and FWI discussion.

REFERENCES

Baumstein, A., Anderson, J.E., Hinkley, D.L. and Krebs, J.R., 2009. Scaling of the objective function gradient for full wavefield inversioin. Expanded Abstr., 79th Ann. Internat. SEG Mtg., Houston: 2243-2247.

Boonyasiriwat C., Valasek, P., Routh, P., Cao, W.P., Schuster, G.T. and Macy, B., 2009. An efficient multiscale method for time-domain waveform tomography. Geophysics, 74(6): WCC59-WCC68.

Brossier, R., Operto, S. and Virieux, J., 2009a.Two-dimensional seismic imaging of the Valhall model from synthetic OBC data by frequency-domain elastic full-waveform inversion. Expanded Abstr., 79th Ann. Internat. SEG Mtg., Houston: 2293-2297.

Brossier, R., Operto, S. and Virieux, J., 2009b. Seismic imaging of complex onshore structures by 2D elastic frequency-domain full-waveform inversion. Geophysics, 74(6): WCC105-WCC118.

Bunks, C., Saleck, F.M., Zaleski, S. and Chavent, G., 1995. Multiscale seismic waveform inversion. Geophysics, 60: 1457-1473.

Bunting, T., Lim, B.J., Lim, C.H., Kragh, E., Gao, R.T., Yang, S.K., Zhang, Z.B., Xie, Y.H. and Li, L., 2011. Marine broadband case study offshore China. First Break, 29(9), 67-74.

Crase, E., Pica, A. and Noble, M., 1990. Robust elastic nonlinear waveform inversion: Application to real data. Geophysics, 55: 527-538.

Forgues, E. and Lambaré, G., 1997. Parameterization study for acoustic and elastic ray and Born inversion. J. Seismic Explor., 6: 253-278.

Hill, D., Combee, C. and Bacon, J., 2006. Over/under acquisition and data processing: The next quantum leap in seismic technology? First Break, 24(6): 81–96.

Köhn, D., Nil, D.D., Kurzmann, A., Przebindowska, A. and Bohlen, T., 2012. On the influence of model parametrization in elastic full waveform tomography. Geophys. J. Internat., 191: 325-345.

Lailly, P., 1983. The seismic inverse problem as a sequence of before-stack migrations. Conference on Inverse Scattering: Theory and Application. SIAM: 206-220.

Liu Q.Y. and Tromp, J., 2006. Finite-frequency kernels base on adjoint methods. Bull. Seismol. Soc. Am., 96: 2383-2397.

Mora, P., 1987. Nonlinear two-dimensional elastic inversion of multi-offset seismic data. Geophysics, 52: 1211-1228.

Moldoveanu, N., Combee, L., Egan, M., Hampson, G., Sydora, L. and Abriel, W., 2007. Over/under towed-streamer acquisition: a method to extend seismic bandwidth to both higher and lower frequencies. The Leading Edge, 26: 41-58.

Nocedal, J. and Wright, S., 2006. Numerical Optimization, 2nd ed. Springer Verlag, Operations Research and Financial Engineering, New York.

Operto, S., Gholami, Y., Prieux, V., Ribodetti, A., Brossier, R., Metivier, L. and Virieux, J., 2013. A guided tour of multiparameter full waveform inversion with multicomponent data: from theory to practice. The Leading Edge, 32: 1040-1054.

Özdemir, K., Caprioli, P., Özbek, A., Kragh, E. and Robertsson, J., 2008. Optimized deghosting of over/under towed streamer data in the presence of noise. The Leading Edge, 27: 190-199.

Plessix, R.E. and Cao, Q., 2011. A parametrization study for surface seismic full waveform inversion in an acoustic vertical transversely isotropic medium. Geophys. J. Internat., 185: 539-556.

Pratt, R.G., Shin, C. and Hicks, G.J., 1998. Gauss-Newton and full Newton methods in frequency-space seismic waveform inversion. Geophys. J. Internat., 133: 341-362

Ravasi, M., Vasconcelos, I., Curtis, A. and Kritski, A., 2015a. Vector-acoustic reverse time migration of Volve ocean-bottom cable data set without up/down decomposed wavefields. Geophysics, 80(4): S137-S150.

Ravasi, M., Vasconcelos, I., Curtis, A. and Kritski, A., 2015b. A practical approach to vector-acoustic imaging of primaries and free-surface multiples. Workshop, 77th EAGE Conf., Madrid.

Ren, Z. and Liu, Y., 2016. A hierarchical elastic full-waveform inversion scheme based on wavefield separation and the multistep-length approach. Geophysics, 81(3), 99-123.

Sirgue, L. and Pratt, R.G., 2004. Efficient waveform inversion and imaging: A strategy for selecting temporal frequencies. Geophysics, 69: 231-248.

Sears, T.J., Singh, S.C. and Barton, P.J., 2008. Elastic full waveform inversion of multi-component OBC seismic data. Geophys. Prosp., 56: 843-862,

Sirgue, L., Etgen, J. and Albertin, U., 2008. 3D frequency-domain waveform inversion using time-domain finite-difference methods. Extended Abstr., 70th EAGE Conf., Rome: F022.

Symes, W.M., 2007. Reverse-time migration with optimal checkpointing. Geophysics, 72(5): SM213-SM221.

Shipp, R.M. and Singh, S.C., 2002. Two-dimensional full wavefield inversion of wide-aperture marine seismic streamer data. Geophys. J. Internat., 151: 325-344.

Sandberg, K. and Beylkin, G., 2009. Full wave equation depth extrapolation for migration. Geophysics, 74: WCA121-WCA128.

Sonneland, L., Berg, L., Eidsvig, P., Haugen, A., Fotland, B. and Vestby, I., 1986. 2D deghosting using vertical receiver arrays. Expanded Abstr., 56th Ann. Internat. SEG Mtg., Houston: 516-519.

Tarantola, A., 1984. Inversion of seismic reflection data in the acoustic approximation. Geophysics, 49: 1259-1266.

Tarantola, A., 1986. A strategy for nonlinear elastic inversion of seismic reflection data. Geophysics, 51: 1893-1903.

Vasconcelos, I., 2013. Source-receiver, reverse-time imaging of dual-source, vector-acoustic seismic data. Geophysics, 78(2): WA123-WA145.

Virieux, J., 1984. SH-wave propagation in heterogenerous media: Velocity-stress finite-difference method. Geophysics, 49: 1933-1957.

Virieux, J. and Operto, S., 2009. An overview of full-waveform inversion in exploration geophysics. Geophysics, 74(6): WCC1-WCC26.

Wu, R. and Aki, K., 1985. Scattering characteristics of elastic waves by an elastic heterogeneity. Geophysics, 50: 582–595.

Wang, T.F. and Cheng, J.B., 2017. Elastic full waveform inversion based on mode decomposition: the approach and mechanism. Geophys. J. Internat., 209: 606-622.

Wang, B.L., Gao, J.H., Chen, W.C. and Zhang, H.L., 2012. Efficient boundary storage strategies for seismic reverse time migration. Chin. J. Geophys. (in Chinese), 55: 2412-2421

Wang, J., Zhou, H., Tian, Y.K. and Zhang, H.J., 2012. A new scheme for elastic full waveform inversion based on velocity-stress wave equations in time domain. Expanded Abstr., 82nd Ann. Internat. SEG Mtg., Las Vegas: 1-5.

You, J Ch., G.C. Li, X.W. Liu, W.G. Han, G.D. Zhang, 2016. Full-wave-equation depth extrapolation for true amplitude migration based on a dual-sensor seismic acquisition system: Geophysical Journal International, 204(3), 1462–1476.

You, J.Ch., Liu, X.W. and Wu, R.S., 2017. First-order acoustic wave equation reverse time migration based on the dual-sensor seismic acquisition system. Pure Appl. Geophys., 174: 1345-1360.

Zhou, H., Takenaka, J.E. and Tanaka, T., 2008. A breast imaging model using microwaves and time domain three dimensional reconstruction method. Progr. Electromagnet. Res., 93: 57-70.

APPENDIX

ADJOINT STATE WAVE EQUATIONS AND GRADIENTS FOR ACOUSTIC FULL-WAVEFORM INVERSION BASED ON THE VELOCITY-STRESS EQUATIONS

In this Appendix, we derive the adjoint state wave equations and gradients for acoustic full-waveform inversion based on the velocity-stress equations.

We rewrite eq. (1) and generalize it using matrix-vector notation in simple form as:

$$L(\rho,\kappa)S = f. \tag{A-1}$$

where $S=(V_x,V_z,P)^T$, $f=(0,0,f_{xx})^T$, T denotes the matrix transpose operator, f is the source item, and

$$L(\rho,\kappa)=\begin{bmatrix} \rho\dfrac{\partial}{\partial t} & 0 & -\dfrac{\partial}{\partial x} \\ 0 & \rho\dfrac{\partial}{\partial t} & -\dfrac{\partial}{\partial z} \\ -\kappa\dfrac{\partial}{\partial x} & -\kappa\dfrac{\partial}{\partial z} & \dfrac{\partial}{\partial t} \end{bmatrix} \tag{A-2}$$

The model parameters can be splinted into background and perturbation components m and δm. The background and perturbation components of the model parameters are $(\rho,\kappa)^T$ and $(\rho+\delta\rho,\kappa+\delta\kappa)^T$, and the corresponding wavefields are represented as $S=(V_x,V_z,P)^T$ and $\delta S=(\delta V_x,\delta V_z,\delta P)^T$, respectively. Thus the following expression is obtained

$$L(\rho+\delta\rho,\kappa+\delta\kappa)^T(S+\delta S)=f. \tag{A-3}$$

Subtracting eq. (A-1) from (A-3) and ignoring the high-order terms based on the Born approximation, we can obtain the perturbed wavefield by following eqs. (A-4):

$$L(\rho,\kappa)\delta S=-L_{\rho}^{'}S\delta\rho-L_{\kappa}^{'}S\delta\kappa. \tag{A-4}$$

where

$$L_{\rho}^{'}=\begin{bmatrix}\frac{\partial}{\partial t} & 0 & 0\\ 0 & \frac{\partial}{\partial t} & 0\\ 0 & 0 & 0\end{bmatrix}, L_{\kappa}^{'}=\begin{bmatrix}0 & 0 & 0\\ 0 & 0 & 0\\ -\frac{\partial}{\partial x} & -\frac{\partial}{\partial z} & 0\end{bmatrix} \tag{A-5}$$

According to the adjoint state method, the adjoint state operator $L(\rho,\kappa)^{*}$ satisfies the following equation (Tarantola, 1986):

$$\left\langle L(\rho,\kappa)^{*}s,\delta S\right\rangle=\left\langle s,L(\rho,\kappa)\delta S\right\rangle \tag{A-6}$$

where $s=(u_x,u_z,p)^{T}$ is the adjoint state wavefield vector.

With the initial condition

$$\delta S\big|_{t=0}=0. \tag{A-7}$$

and the boundary condition

$$\delta S\big|_{z=0}=0. \tag{A-8}$$

We deduce the adjoint operator using the property of integration by parts. It can be expressed as

$$L(\rho,\kappa)^{*}=\begin{bmatrix}\rho\frac{\partial}{\partial t} & 0 & -\kappa\frac{\partial}{\partial x}\\ 0 & \rho\frac{\partial}{\partial t} & -\kappa\frac{\partial}{\partial z}\\ -\frac{\partial}{\partial x} & -\frac{\partial}{\partial z} & \frac{\partial}{\partial t}\end{bmatrix}. \tag{A-9}$$

Thus, the adjoint state wave equations can be expressed as

$$\begin{cases}\rho\dfrac{\partial u_x}{\partial t}=\kappa\dfrac{\partial p}{\partial x}.\\ \rho\dfrac{\partial u_z}{\partial t}=\kappa\dfrac{\partial p}{\partial z}.\\ \dfrac{\partial p}{\partial t}=(\dfrac{\partial u_x}{\partial x}+\dfrac{\partial u_z}{\partial z}).\end{cases} \tag{A-10}$$

In our acoustic FWI, the objective function is set as L_2 objective function:

$$E = \frac{1}{2}\left\| S(m)^{cal} - S^{obs} \right\|_2^2 \tag{A-11}$$

where the $S^{cal}(m)$ is the calculated data with model m and the S^{obs} is the observed data, respectively.

The gradient of the objective function with respect to the model parameter *m* can be derived from the following equation:

$$\frac{\partial E}{\partial m} = \left\langle \frac{\partial S(m)^{cal}}{\partial m}, S(m)^{cal} - S^{obs} \right\rangle \tag{A-12}$$

Taking the derivative of eq. (A-1), we get

$$\frac{\partial L}{\partial m} S(m) + L \frac{\partial S(m)}{\partial m} = 0 \tag{A-13}$$

,

which can be rearranged to give

$$\frac{\partial S(m)}{\partial m} = -L^{-1}(m) \frac{\partial L}{\partial m} S(m) \tag{A-14}$$

.

Plugging eq. (A-14) into eq. (A-12), we get

$$\frac{\partial E}{\partial m} = -\left\langle \frac{\partial L}{\partial m} S(m), \left(L^{-1}(m)\right)^* \Delta S \right\rangle \tag{A-15}$$

,

where * denotes the adjoint, $\Delta S = S(m)^{cal} - S^{obs}$ is the residual vector.

In the context of acoustic FWI, we denote $s = \left(L^{-1}(m)\right)^* \Delta S$ as the solution of the adjoint equations with the residual seismograms acting as virtual sources

$$L(\rho, \kappa)^* s = \Delta S \tag{A-16}$$

.

For $m = (\rho, \kappa)^T$, the gradient in eq. (A-15) can be written as

$$\frac{\partial E}{\partial \rho} = -\left\langle \frac{\partial L}{\partial \rho} S(\rho), s \right\rangle = -\left\langle \begin{pmatrix} \frac{\partial}{\partial t} & 0 & 0 \\ 0 & \frac{\partial}{\partial t} & 0 \\ 0 & 0 & 0 \end{pmatrix} \begin{pmatrix} V_x \\ V_z \\ P \end{pmatrix}, \begin{pmatrix} u_x \\ u_z \\ p \end{pmatrix} \right\rangle = -\int_0^T (u_x \frac{\partial V_x}{\partial t} + u_z \frac{\partial V_z}{\partial t}) dt$$

(A-17)

and

$$\frac{\partial E}{\partial \kappa} = -\left\langle \frac{\partial L}{\partial \kappa} S(\kappa), s \right\rangle = -\left\langle \begin{pmatrix} 0 & 0 & 0 \\ 0 & 0 & 0 \\ -\frac{\partial}{\partial x} & -\frac{\partial}{\partial z} & 0 \end{pmatrix} \begin{pmatrix} V_x \\ V_z \\ P \end{pmatrix}, \begin{pmatrix} u_x \\ u_z \\ p \end{pmatrix} \right\rangle = \int_0^T p(\frac{\partial V_x}{\partial x} + \frac{\partial V_z}{\partial z}) dt$$

(A-18)